PCCP

ROYAL SOCIETY OF CHEMISTRY

PAPER

View Article Online
View Journal | View Issue

Cite this: *Phys. Chem. Chem. Phys.*, 2026, **28**, 7352

Nano IR spectroscopy on silicon-supported organic–inorganic hybrid materials

Carolin Mehrmann,[a] Jacob Johny,[b] Petra Ebbinghaus,[a] Martin Hammerschmidt,[c] Ankita Das,[a] Xin Wei,[d] Marc F. Tesch[b] and Martin Rabe*[a]

Received 2nd October 2025,
Accepted 23rd February 2026

DOI: 10.1039/d5cp03815d

rsc.li/pccp

We study a recently developed model system for multifunctional catalysts consisting of Ru nanoparticle covered supported ionic liquid phases (RuNP@SILP). In order to learn about the nanostructure of this system photothermal nano-IR spectroscopy (AFM-IR) is applied here. Studying such molecular monolayers using AFM-IR has proven challenging with success mostly limited to gold substrates, due to gold's intrinsic field enhancement. In contrast, the application of AFM-IR to ultrathin layers on Si|SiO$_2$ substrates as used in this study for the SILPs has not yet been reported. Here, we approach this challenge and employ AFM-IR and nano-optics simulations using the finite element method. We demonstrate that good S/N ratio AFM-IR spectra can be obtained for monolayers on Si|SiO$_2$ and that, in the case of metal overlayers, the underlying monolayer's IR absorbance is determined by the structure of the metal overlayer. Ultimately, this approach leads to novel insights on the nanostructure of SILPs and RuNP@SILPs and can be applied more broadly to the larger class of molecularly modified surfaces.

Introduction

Ultrathin molecular self-assembled monolayers (SAMs) offer a convenient means to tailor application specific physical and chemical surface properties. Hence, they are applied in manyfold functional materials in diverse fields such as biosensing, corrosion and biofouling protection, organic electronic devices, as well as catalysis.[1–3] Despite their wide ranging applications, the nanostructure of such applied monolayers is rarely studied although it must be assumed that this structure strongly influences the materials' functionality. Here, we focus on hybrid materials consisting of supported ionic liquid phases (SILP) and metal nanoparticles (NPs) that have been widely used as multifunctional catalysts.[3,4] In these systems, ionic liquid (IL) monolayers on silica powder are reported to act as nanoparticle stabilisers. Thus, such systems are intended to bridge homogeneous (molecular) and heterogeneous (material) catalysis, and can be tailored for activity and selectivity by using different combinations of nanoparticles, molecular modifiers and supports. To better understand this emerging type of catalysts, model systems employing Ruthenium nanoparticles (RuNPs) and imidazolium based ILs have been recently prepared on flat silicon wafers instead of typically used silica powders.[5] The idea behind this approach was to create model systems on (ultra) flat substrates, that enable the nanostructural study of the RuNP@SILP system by a wider variety of analytical techniques that require such sample geometry. Fig. 1 shows a simplified scheme of the model system depicting this approach. Here, we aim to continue this work by the application of photothermal nano-IR spectroscopy, also called atomic force microscope-infrared spectroscopy (AFM-IR) to the SILP and RuNP@SILP systems in order to obtain a more detailed understanding of their nanostructure.

However, despite the increasing availability of commercial AFM-IR setups with the necessary top-side illumination for over 10 years,[6] reports on the study of ultrathin molecular monolayers have remained scarce, which might be a consequence of

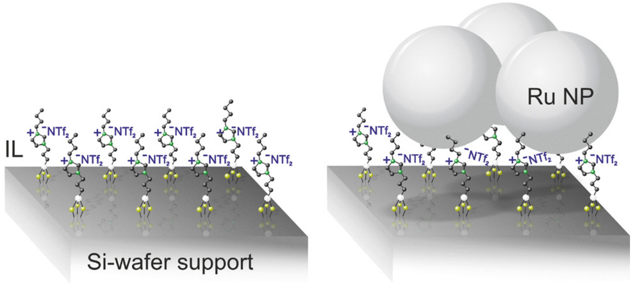

Fig. 1 Scheme of imidazolium-based SILP and RuNP@SILP.

---

[a] *Max Planck Institute for Sustainable Materials, Max-Planck-Str. 1, 40237 Düsseldorf, Germany. E-mail: m.rabe@mpi-susmat.de*
[b] *Max Planck Institute for Chemical Energy Conversion, Stiftstraße 34-36, 45470 Mülheim an der Ruhr, Germany*
[c] *JCMwave GmbH, Bolivarallee 22, 14050 Berlin, Germany*
[d] *Institute of Inorganic Chemistry (IAC), RWTH Aachen University, Landoltweg 1a, 52074 Aachen, Germany*

the intrinsic challenges such samples pose to the method.[7–11] In this regard, the most significant challenge to mention is the low signal intensity that characterizes monolayers. To overcome this challenge, researchers used electromagnetic field enhancement governed by gold (Au) substrates and tips to increase the signal intensity required for monolayer detection, which as a drawback limits the material composition for AFM-IR analysis. However, recent results on highly oriented pyrolytic graphite (HOPG) suggest that other non-metallic substrates may also be suitable for such highly sensitive measurements.[8] SAMs on Si|SiO_2 such as the SILP and RuNP@SILP investigated here are widely used and studied.[12] Therefore, the applicability of the AFM-IR methodology to monolayers on Si|SiO_2 substrates would extend the toolbox of highly surface sensitive analysis methods and would represent a significant progress in this field.

We first approach this issue by finite-element-method (FEM) simulations to asses the expected field enhancement of ultrathin organic layers on Si|SiO_2 substrate and the influence of possible metal overlayer structures of RuNP@SILP. This is followed by a demonstration of the successful implementation by AFM-IR measurements which yields novel insights into the nanostructure of the sutdied SILP and RuNP@SILP systems.

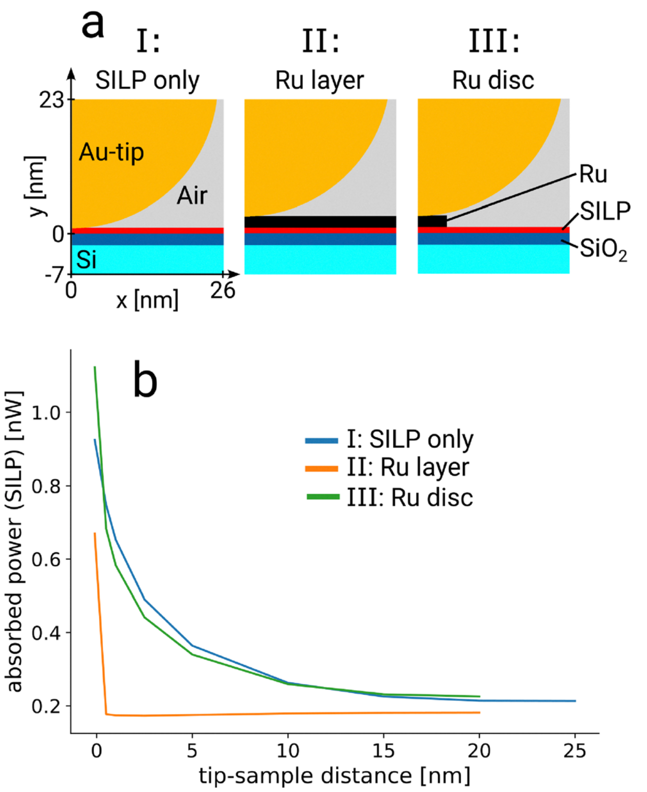

Fig. 2 2-D layout before rotation around *y*-axis (a) used for FEM modeling. Results of FEM modeling. Power absorbed by SILP depends on the tip-sample distance (b).

Results and discussion

Metal overlayers influence AFM-IR spectral intensities

To simulate and compare the measurable signal intensities of AFM-IR measurements on RuNP@SILP and SILP prepared on ultraflat silicon wafers, we employed FEM. This method allows to study the field intensities and the absorbance within the monolayers of interest and to compare different sample structure scenarios. To that end under a hemispherical Au AFM tip, we constructed three different models that represent possible states of the RuNP@SILP and the pure SILP systems under study (Fig. 2a): (I) a SILP monolayer on Si|SiO_2; (II) a continuous, metallic Ru layer on system I; and (III) a Ru disc on system I, modelling a non-continous nano particle layer. Fig. 2a shows the initial 2D layouts which were converted to 3D models by rotation around the *y*-axis. The modeled layer thicknesses match the SILP and RuNP@SILP sample structures determined from results of spectroscopic ellipsometry measurements. The SILP thicknesses was modeled with 1 nm close to the molecular length of the employed IL of about 1.2 nm and in the range of ellipsometric thicknesses found in the range 1 nm to 2 nm. The modeled metal overlayers were 2 nm thick and the Ru disc featured a radius of 5 nm.[5] The *x*–*y* plane represented the plane of incidence, with the light entering at an angle of 70 to the *y*-axis.

The absorbed power in the SILP obtained from the FEM simulations (Fig. 2) represents the absorbance within the monolayer and is proportional to the measured signal in AFM-IR.[6,13] Typically, we employ tapping AFM-IR on molecular monolayers[7] to reduce lateral forces on the sample during the measurements. In this mode, the gold covered AFM tip oscillates over the sample and is hence only shortly in direct repulsive contact. Depending on the laser configuration used, typically employed duty cycles are up to 5%, meaning that absorbance can in principle also occur when the tip is not in direct contact with the sample. Also, another tapping AFM based nano-IR technique, photoinduced force microscopy (PiFM), works at higher tip-sample distances in the attractive regime.[14,15] Therefore, the variation of the absorbance due to the tip oscillation is worth investigating. This scenario was modeled by varying the tip-sample distance ($d_{\text{t-s}}$), which was found to strongly influence the field enhancement and absorbance within the monolayer (Fig. 2). The distance dependence arises because the gold coated AFM-tip causes a local field enhancement at its direct vicinity. Naturally, the absorbance was found to be maximum at direct contact with slight indent ($d_{\text{t-s}} = -0.1$ nm) for all studied models. Here, contact and indentation at negative $d_{\text{t-s}}$ was modeled by the unaltered tip indenting and thereby slightly deforming the first layer. At higher $d_{\text{t-s}}$ the absorbance drops and for $d_{\text{t-s}} \geq 15$ nm it is virtually equivalent to the absorbance at absent tip ($d_{\text{t-s}} = 25$ nm for SILP only (I); $d_{\text{t-s}} = 20$ nm for Ru containing models (II & III)).

The local enhancement within the SILP layer (0.1 nm underneath the SILP surface) is depicted in Fig. 3 by means of the calculated local field intensity enhancement factor (LFIEF) in the *xz*-plane, *i.e.*, parallel to the interface. For the pure SILP, the local field enhancement is located close to the tip apex and increasing the tip-sample distance leads to a blurring of the initially sharp enhancement regions (Fig. 3a and b).

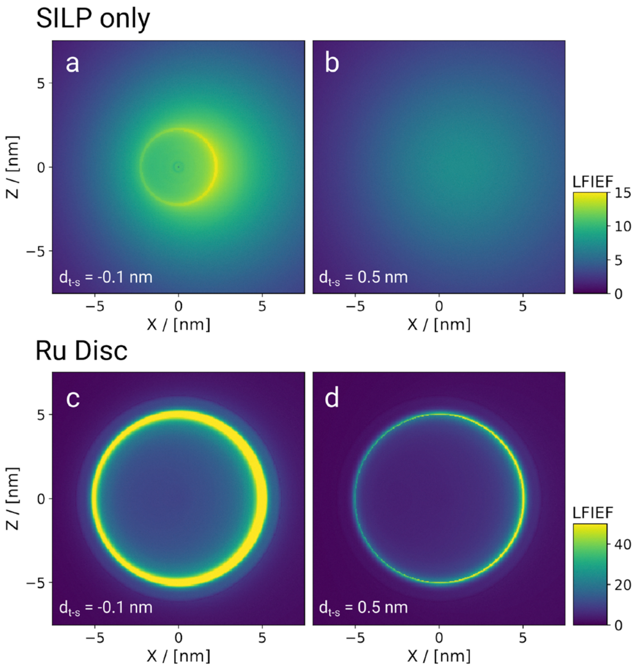

Fig. 3 Local field intensity enhancement maps at y = 0.9 nm for SILP only (I: a, b) and Ru Disc (III: c, d) models. Maximum local field intensity enhancement factor (LFIEF) values in the images in Fig. 3c and d go up to about 250 and 200, the smaller scale was chosen for visibility and comparability reasons.

A comparison of the power absorption in the SILP with a continuous Ru overlayer (model II) and without (model I) shows that only in case of direct contact, significant absorbance occurs underneath the Ru (Fig. 2) because field enhancement from the tip is transmitted over the Ru layer into the SILP monolayer (see also SI, Fig. S1). In the case of non-contact ($d_{t\text{-}s} \geq 0.5$ nm), the local field intensity below the continuous Ru is quenched due to the high extinction coefficient of the metal (SI, Fig. S1c). This shielding causes that the total absorbance for $d_{t\text{-}s} \geq 0.5$ nm under the continuous Ru layer is even lower than that of pure SILP even with absent tip ($d_{t\text{-}s}$ = 25 nm) (Fig. 2).

This situation changes significantly when the Ru layer is not continuous, modeled here by a disc-shaped RuNP (model III). The Ru disc model features an absorbance-$d_{t\text{-}s}$ curve, comparable to the SILP only system (model I, Fig. 2). The origin of the absorbance is a significant field enhancement at the edges of the Ru disc (Fig. 3c and d). It is noted that the maximum LFIEF values in the images in Fig. 3c and d go up to about 250 and 200, respectively (compare also SI, Fig. S1d), but a smaller scale was chosen for better comparability and depiction of the regions with lower enhancement. Thus, especially in the case of contact between the Au tip and the Ru disc ($d_{t\text{-}s} = -0.1$ nm), significant field enhancement is transmitted from the tip *via* the Ru disc into the SILP.

The real three dimensional shape of the Ru NPs in these RuNP@SILP system is not exactly known, but is most likely not a perfect disc as in model III. In transmission electron microscopy images the particles appear as small islands which are connected together with having some undeposited areas in between.[5] This observation is in line with a Volmer Weber like growth of metal islands from the gas phase, which would lead to more rounded particles.[16] Additional simulations of hemispherical- and hemiellipsoidal-shaped NPs gave qualitatively very similar results to model III while only smaller quantitative differences were found (SI, Fig. S2). This shows that transmission of the field enhancement into the SILP is a general phenomenon that is independent on the precise NP shape.

Furthermore, the models I–III on Si|SiO$_2$ were compared with a model representing monolayers on gold substrates which is the commonly reported substrate in AFM-IR monolayer studies. The absorbed power in an ultrathin layer on gold substrate was found to be larger than on Si|SiO$_2$ by a maximum factor of *ca.* 8 at contact. The difference in absorbance between the models decreased with increasing $d_{t\text{-}s}$ (SI, Fig. S3).

The theoretical approach taken here is simplified such that it exclusively studies electromagnetic field absorbance as the initial necessary condition for successful AFM-IR measurements. The technical implementation is based on the thermal expansion of the material caused by the absorbed energy, which generates a mechanical signal that can be measured by AFM. Therefore, other material properties such as the thermal expansion coefficient, and the heat diffusion significantly influence both the signal intensity[13] and the lateral resolution.[17] Typically, organic/polymer materials have larger thermal expansion coefficients, while many inorganic materials and metals virtually do not generate signals in photothermal nano-IR due to their low thermal expansion coefficient. Therefore, in our system, the main mechanical signal is assumed to arise exclusively from the SILP. Furthermore, the thermal and mechanical properties of the SILP can be assumed to be homogeneous across the sample. These two facts generally justify the use of our simplified approach. A more detailed analysis of the influence of these material factors, especially with regard to the locally heterogeneous metal NPs, could shed light on their impact on lateral AFM-IR resolution. However, this is not considered necessary for the studied RuNP@SILP system at the current stage because, as discussed in the next section, it contains features that cannot currently be resolved laterally using AFM imaging.

Taken together, the results of the FEM simulations show that although the enhancement from the gold substrate is helpful for improving the AFM-IR signal intensity, Si|SiO$_2$ substrates also yield absorptions in the molecular layer that should be detectable by AFM-IR. Furthermore, on monolayers covered with non-continuous metal nanoparticle overlayers, the absorbance of the intermittend monolayer can be detected due to the transmittance of the field enhancement *via* the metal into the organic layer. A thin continouos metal layer in contrast is not expected to allow for a measurable SILP signal in tapping AFM-IR. In the following, we report experimental results that prove these theoretical findings.

AFM-IR detects SILP aggregates

Experimentally, the SILP on ultra flat Si|SiO$_2$ wafers was studied by using tapping-AFM-IR. An exemplary AFM topography image (Fig. 4a), shows a relatively smooth surface with dot like features of different heights, varying for example between

5.5 to 9 nm as revealed by the line scans (Fig. 4c). The number of these features was found to vary over samples and positions and their presence was confirmed for three independently prepared samples. Apart from these features, the surface topography appears very flat as would be expected for either homogeneous coverage by the monolayer or absence of it. Hence, the presence of the SILP monolayer cannot be undoubtedly concluded from the AFM observations only, because reference AFM measurements of the pure ultraflat Si|SiO$_2$ yielded a similarly flat surface structure except for the dot-like features observed on SILP (SI, Fig. S4).

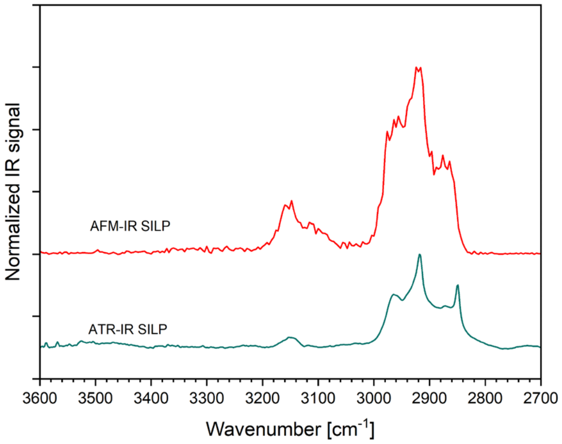

Fig. 5 Comparison of AFM-IR and ATR-IR spectra of SILP. ATR-IR data is the same as previously published.[5]

The confirmation of a homogeneous coverage was achieved by AFM-IR, which in addition yielded local IR-nanospectra of the SILP as depicted in Fig. 5. The direct comparison of the AFM-IR spectrum with an IR spectrum of a SILP recorded by the attenuated total reflection (ATR-IR) technique under similar conditions in a previous study[5] reveals striking similarities (see also peak positions in Table 1). Both spectra show peaks in the range from 3200 to 2800 cm^{-1} typical for the expected C–H stretching modes (ν). The C–H stretching of the aromatic imidazole ring should typically appear between 3000 cm^{-1} to 3200 cm^{-1} and is found at about 3150 cm^{-1} in AFM-IR and ATR-IR spectra, while the aliphatic antisymmetric and symmetric C–H stretching modes are found below 3000 cm^{-1} (Table 1). It is noted that the relative spectral intensities of the peaks obtained for AFM-IR spectra varied by sample and positions while the peak positions did not shift strongly (compare for instance Fig. 5 and SI, Fig. S5a). In ultrathin films both, the polarisation of the field and the molecular orientation with respect to the field strongly influence the peak ratios in the ν(CH) region.[18,19] We expect that for AFM-IR on a nonmetallic substrate the polarisation of the near field strongly depends on the nanoscale tip shape. Hence, we consider variations in tip shape as well local nano scale variations of molecular orientations as likely causes for the observed peak ratio differences.

Nevertheless, the co-occurrence of the aromatic and the aliphatic stretching vibrations (Table 1) in the spectra confirm

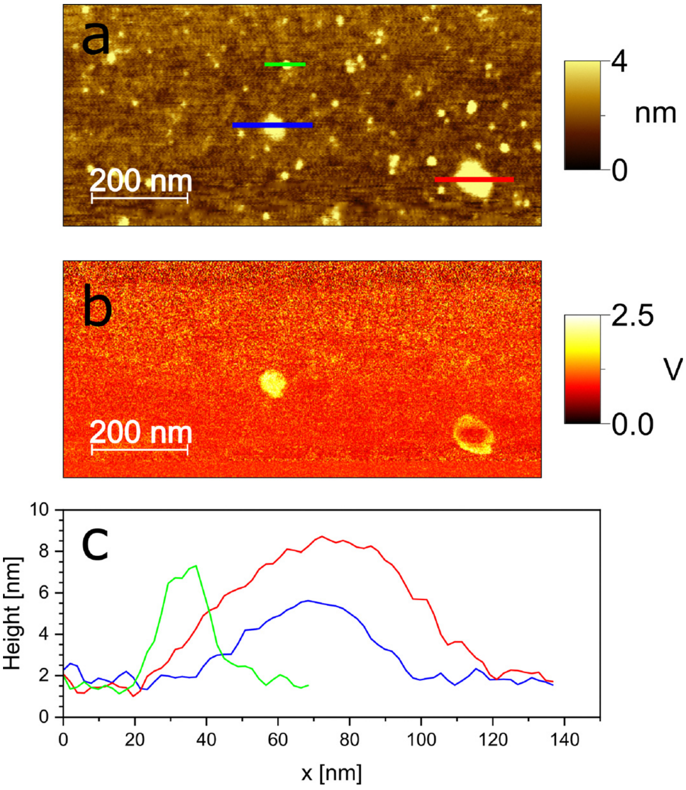

Fig. 4 AFM-IR results on a SILP sample: Height image (a) and IR Amplitude scanned at 2956 cm^{-1} (b), linescans of features (c) line colors corresponding to the colored lines in a.

Table 1 Major IR peak positions (cm^{-1}) and their assignments. Peak positions from AFM-IR are approximates due to higher noise and lower resolution. ATR-IR data is the same as previously published.[5]

SILP AFMIR	SILP ATR-IR	Ru@SILP AFMIR	Ru@SILP ATR IR	Assignment
~3152	3150	3152	3149	$\nu(C_{Ar}\text{–}H)$
~3110		~3110		$\nu(C_{Ar}\text{–}H)$
~2964	2964	~2960	2956	$\nu_{as}(C\text{–}H_3)$
~2920	2918	2928	2922	$\nu_{as}(C\text{–}H_2)$
~2864	2849	~2856	2851	$\nu_s(C\text{–}H_2)$

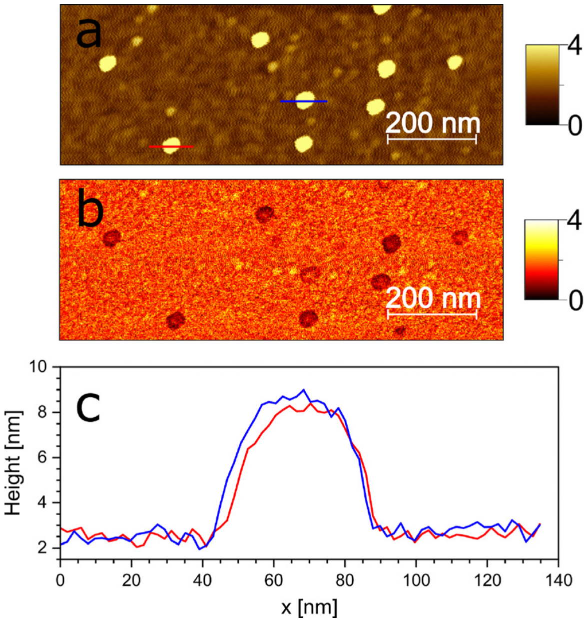

Fig. 6 AFM-IR results on a RuNP@SILP sample: height image (a) and IR Amplitude scanned at 2956 cm^{-1} (b), linescans of features (c) line colors corresponding to the colored lines in a.

the presence of the SILP at the interfaces. Also, the position of the $\nu(C_{Ar}\text{–}H)$ at 3152 cm^{-1} indicates that there is no strong interaction of the imidazole ring with the NTf_2 anion.[20] The slight peak shifts observed in the comparison of AFM-IR and ATR-IR results may be a result of tip sample interactions, since the position and peak width of $\nu(C\text{–}H)$ bands are known to vary with SAM crystallinity. However, this cannot be said with full certainty due to the lower resolution and S/N ratio in AFM-IR, which is why the peak positions in AFM-IR are less certain.

IR imaging at 2956 cm^{-1} revealed a homogenous distribution of IR absorbance over the sample but a higher absorbance was recorded on the dot-like features (Fig. 4b). We interpret this as an indication of ionic liquid material forming multilayer structures on the sample and hence being not directly bound to the SiO_2 interface. The increased absorbance of the $\nu(C\text{–}H)$ bands was also confirmed by local nano IR spectra (SI, Fig. S5). Dhotel *et al.* observed similar features appearing on Silane based self-assembled monolayers with polar tails[21] and also interpreted them as molecular aggregates. Interestingly, on SAMs with apolar tails they did not observe such features indicating electrostatic forces being involved in the aggregate formation. The SILP used here is ionic in nature and hence we consider a similar electrostatically driven aggregate formation as the most probable origin of the observed structures. Taken together, these results show that AFM-IR is able to detect the spectroscopic signals of the SILP monolayer on $Si|SiO_2$ and that the layers are mostly homogenous, except for the appearance of a small fraction of multilayer aggregates.

AFM-IR measures SILP beneath Ru nanoparticles

Deposition of an ultrathin noncontinuous RuNP layer was achieved by a magnetron sputtering deposition for a short duration of 2 s from a Ru-target. Transmission electron microscopy and spectroscopic ellipsometry confirmed that this procedure leads to an evenly distributed coverage of NPs in lateral size ranges of 2 nm to 4 nm in the range 50% to 60% and thicknesses ≤5 nm.[5] The AFM topography scan was found unable to resolve these small nanostructures (Fig. 6a). The gold coated tips used for AFM-IR feature nominal apex diameters of about 50 nm, which is too broad to resolve small dips with expected lateral sizes and depths ≤5 nm. Hence the background of the AFM topography of RuNP@SILP appears comparably smooth as the reference pure ultraflat $Si|SiO_2$ surface (compare SI, Fig. S4).

Apart from the smooth background, the topography reveals further dot like features scattered over the interface with density and sizes varying over samples and positions. The line scans in Fig. 6c indicate that the tip diameter exceeded the lateral feature size and the tip was imaged, however also bigger features were observed at other sample positions (SI, Fig. S6). As for the NP-free SILP, these features showed typically heights of 5 nm to 10 nm. However, in contrast to the NP-free SILP, minor features with increased and dominating features with decreased IR absorbance in the $\nu(C\text{–}H)$ range were observed coincidentally on RuNP@SILP, as is shown by the IR imaging at 2956 cm^{-1} (Fig. 6) as well as local nano IR spectroscopy (SI, Fig. S6). The similarity of size and shape of the dominating features compared to the SILP sample suggests an origin in the SILP formation. A tentative hypothesis for the observed IR absorbance decrease might be that SILP agglomerates affect the distribution of the Ru layer formation in these regions. However, earlier energy-dispersive X-ray spectroscopy (EDX) measurements (see SI of ref. 5 did not provide any conclusive proof), and AFM-IR is unable to provide additional information due to its inherent insensitivity to metals. Therefore, an unambiguous answer to the origin of the observed signal decrease at these specific structures cannot be given at this stage.

When comparing local nano-IR spectra and ATR-IR spectra, obtained under similar conditions, for the RuNP@SILP samples, both spectra show the characteristic peaks in the C–H stretching bands region 2800 to 3200 cm^{-1} as expected from the SILP (Fig. 7). The peaks and their assignments are listed as well in Table 1, for comparison with the SILP samples. Small absorbances above 3200 cm^{-1} are assigned to $\nu(O\text{–}H)$ that may originate from interface Si–OH or adsorbed H_2O. Although the probing geometry differs between the two experiments, *i.e.* the probing beam is internally reflected within the silicon substrate in ATR and external reflection from air is employed in AFM-IR, the spectra are highly similar. Recall that the FEM results discussed

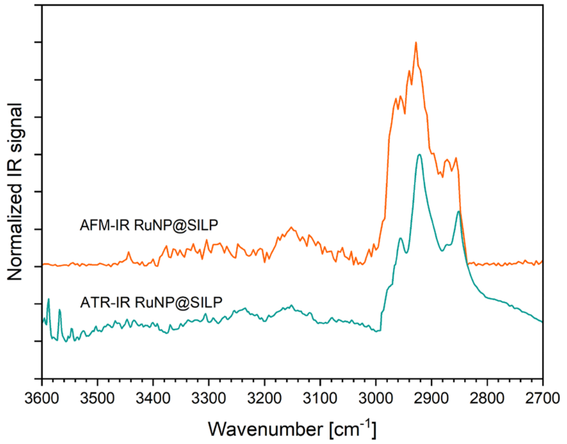

Fig. 7 Comparison of AFM-IR and ATR-IR spectra of RuNP@SILP. ATR-IR data is the same as previously published.[5]

above showed that no strong absorbance is expected for a continuous Ru overlayer. Conversely, this implies that the ability to measure a nano-IR spectrum of the SILP interlayer, as demonstrated here, is a consequence of the discontinuity of the Ru NP film.

Conclusions

This work elucidates the nano structure of complex ultra thin layer arrangements on ultraflat Si|SiO_2 demonstrated on a model system for heterogenous catalysis. We theoretically and experimentally extended the applicability of the AFM-IR method to ultrathin molecular layers on Si|SiO_2 and to ultrathin intermediate molecular layers covered by metal overlayers. The latter structures are proposed to only give measurable signals for discontinuous NP coverages as indicated by FEM simulations. The studied SILP were found to be mostly homogeneous monolayers with a small fraction of multilayer aggregates in the form of circular features whose number and distribution varied across the investigated samples. On RuNP@SILP, the ultrathin ruthenium metal layer itself could not be resolved by AFM-IR, however the SILP interlayer was clearly detected. The RuNP@SILP samples showed additional bigger inorganic features possibly consisiting of Ru.

Taken together, the results prove that AFM-IR spectroscopy can be successfully applied on Si|SiO_2 as substrate modified with SAMs and partially covered by metal nanoparticles. Furhter, these studies highlight the importance of nano-structural analysis of such structures, since unexpected structural variation, such as multilayer formation, may emerge that could affect the functionality of the material. In this regard, the applicability of AFM-IR to a variety of substrates and layer structures significantly expands the scope of this method in this field.

Materials and methods

Finite element modeling of near field optics

The JCMsuite software package (Ver. 5.2.4) was used for finite element modeling of the near field close to the AFM-tip and the sample. The layouts were constructed as 2D cross-section in the xy-plane and converted to 3D models by rotation around the y-axis. The substrates were modeled in air by a semi infinite slab of Si covered by a 2 nm thick slab of SiO_2. For comparison also a model with a semi-infinite gold slab as substrate was used (SI, Fig. S3). On the substrate the ionic liquid monolayer was modeled as material with isotropic refractive index n = 1.5 and extinction coefficient k = 0.1[18] of 1 nm thickness. The IL layer was covered either by a complete Ru layer of 2 nm thickness or a 2 nm thick disc with a radius of 5 nm. Rounded shaped Ru particles were modeled by a hemisphere with a radius of 2 nm and a hemiellipsoid with a radius of 2 nm in y-direction and 4.5 nm in x- and z-directions (SI, Fig. S2). The AFM tip was modeled as gold hemisphere with a radius of 25 nm. The tip-sample distance ($d_{\text{t-s}}$) was varied from contact/slight indent with the unaltered tip deforming the first layer ($d_{\text{t-s}} = -0.1$ nm) to absent tip ($d_{\text{t-s}}$ = 25 nm for SILP only model, $d_{\text{t-s}}$ = 20 nm for model with Ru). Air was modeled as transparent material with refractive index n = 1. The optical properties of the remaining materials were taken directly or interpolated at 3000 cm^{-1} from available literature for Au: n = 1.37; k = 22.97,[22] Ru: n = 4.12; k = 15.6,[23] Si: n = 3.43; k = 0,[24] and SiO_2: n = 1.41; k = 0.0002.[25] To closely simulate the experimental conditions, described below, the light source was modeled as a p-polarized wave with 3000 cm^{-1} originating in $+x$ direction with an incident angle of 70° with respect to the y-axis. The power flux density of the wave was normalised to 1 W m^{-2} and the absolute power absorbed by the SILP was calculated by scaling the output field absorption of the respective domain to the power density achievable by the employed laser source (200 MW m^{-2}). The local field intensity enhancement factor (LFIEF) was calculated by normalizing the squared norm of the local field strengths at each point in the model to the squared norm of the field strength in absence of any structures. The simulation was set up as scattering problem in the frequency domain that calculated the electric field. The finite element degree used for the simulations was set to 4 after optimization.

Sample preparation

Ultra-flat surfaces were one of the prerequisites to resolve potential monolayer morphologies using the AFM-IR measurements. To that end, ultra-flat silicon wafers purchased from Plano GmbH, Germany (manufactured by Ted Pella Inc., USA, product nr.: 21610-510, 10 × 10 mm, $\langle 100 \rangle$) were used as substrates for the model system. After a treatment with piranha solution (see below) these substrates typically featured an RMS roughness of 0.2 nm to 0.25 nm (see for instance SI, Fig. S4).

The SILP synthesis was carried out as described elsewhere.[5] First, the wafers were ultrasonicated in an acetone bath for 5 min and then dried under a nitrogen flow. Subsequently, the wafer surfaces were hydroxylated using a piranha solution treatment. For this, 5 mL of piranha solution was prepared in a Schlenk flask containing a pre-cleaned wafer by slowly adding 1.5 mL of H_2O_2 into 3.5 mL of H_2SO_4. The solution was then heated to 90 °C for one hour. After cooling down, the wafers were washed under running ultrapure water and then dried under a nitrogen flow. Directly after the piranha treatment, the

SILP synthesis was carried out. For this, 2 mL of toluene and 20 mg of IL ([1-butyl-3-(3-triethoxysilylpropyl)imidazolium]bistriflimide) were mixed in a vial inside a glove box and filled into a Schlenk tube containing a piranha-treated wafer. Then a chemical reaction was set up at 95 °C for 18 hours. After cooling down, the wafers were first washed three times using dichloro methane in an ultrasonic bath for three minutes each, to remove any residual physisorbed IL. Finally, the wafers were dried under vacuum for at least two hours and then stored under an inert atmosphere until used for further analyses. The nanoparticle deposition was performed by a magnetron sputtering process in DC mode using a Pfeiffer Vacuum Classic 250 system. Therefore the samples were transferred into the chamber using a metallic holder. A ruthenium target (99.99% purity, MaTeck GmbH) was used as the ruthenium source for the nanoparticles. The sputtering was done at 100 W for 2 s.

AFM-IR

The AFM-IR measurements were conducted with a nanoIR 3 from Bruker. The instrument includes a tunable pulsed fast-OPO IR-laser operating in the wavenumber range from 2700 cm^{-1} to 3700 cm^{-1} that hits the sample at an angle of 70° to the surface normal. The IR laser was set to p-polarisation and the power was optimised for image or spectral quality in the range 0.8 mW to 6.0 mW with a constant pulse width of 10 ns. The topography, IR-mapping, and point spectra scans were performed in tapping mode with a gold coated silicon cantilever (Tapping Mode NIR2 Probes, PR-EX-TnIR-A-10, Bruker AFM probes, USA) with a nominal fundamental resonance frequency of 75 kHz ± 15 kHz. These tips are sourced from the manufacturer with gold a coating (ellipsometric thickness 70 nm) featuring a nominal tip radius of 20 nm to 35 nm. An image resolution of 512 pt and a scan rate of 1 Hz was used. The samples were measured under a controlled N_2 atmosphere with relative humidity of less than 10%. The phase-locked loop (PLL) mode was used to ensure an independence of the recorded IR signal on the materials' mechanical properties, by tracking the cantilever frequency and keeping it aligned with the repetition rate of the OPO laser at *ca.* 189 kHz.

Author contributions

Conceptualization: JJ, MFT, and MR; methodology: MH, JJ, MFT and MR; software: MH and MR; formal analysis: CM, AD and MR; investigation: CM, JJ, PE, AD, XW and MR; supervision and funding acquisition: MFT and MR; writing – original draft: CM and MR; writing – review & editing: all authors.

Conflicts of interest

There are no conflicts to declare.

Data availability

The raw data of the published material is available *via* the Edmond Repository at: https://doi.org/10.17617/3.KXJYIU.

Supplementary information (SI): supporting FEM results and supporting AFM-IR results. See DOI: https://doi.org/10.1039/d5cp03815d.

Acknowledgements

The authors acknowledge financial support by the Max Planck Society and Deutsche Forschungsgemeinschaft (DFG, German Research Foundation), under Germany's Excellence Strategy – Exzellenzcluster 2186 "The Fuel Science Center", no. 390919832. This work is funded by the Deutsche Forschungsgemeinschaft (DFG, German Research Foundation) under Germany's Excellence Strategy – EXC 2033 – 390677874 – RESOLV. Open Access funding provided by the Max Planck Society.

References

1 M. Li, M. Liu, F. Qi, F. R. Lin and A. K.-Y. Jen, *Chem. Rev.*, 2024, **124**, 2138–2204.
2 S. Zhang, R. Geryak, J. Geldmeier, S. Kim and V. V. Tsukruk, *Chem. Rev.*, 2017, **117**, 12942–13038.
3 A. Bordet and W. Leitner, *Acc. Chem. Res.*, 2021, **54**, 2144–2157.
4 A. Bordet, G. Moos, C. Welsh, P. Licence, K. L. Luska and W. Leitner, *ACS Catal.*, 2020, **10**, 13904–13912.
5 J. Johny, S. J. L. Anandaraj, C. Mehrmann, X. Wei, A. Das, N. Scheer, Y. Yang, W. Hetaba, P. Ebbinghaus, U. Simon, R. Eichel, F. Hausen, H. Uphoff, H. Mertins, R. K. Campen, Y. Tong, M. Rabe, W. Leitner, A. Bordet and M. F. Tesch, *Adv. Mater. Interfaces*, 2025, **12**, 2500073.
6 J. Mathurin, A. Deniset-Besseau, D. Bazin, E. Dartois, M. Wagner and A. Dazzi, *J. Appl. Phys.*, 2022, **131**, 010901.
7 N. Samiseresht, G. Figueroa Miranda, A. Das, K. Graef, D. Mayer and M. Rabe, *Small*, 2025, **21**, 2409369.
8 A. Hamadeh, F. Palmino, J. Mathurin, A. Deniset-Besseau, L. Grosnit, V. Luzet, J. Jeannoutot, A. Dazzi and F. Cherioux, *Commun. Chem.*, 2023, **6**, 246.
9 L. Rikanati, S. Dery and E. Gross, *J. Chem. Phys.*, 2021, **155**, 204704.
10 F. Lu, M. Jin and M. A. Belkin, *Nat. Photonics*, 2014, **8**, 307–312.
11 N. Samiseresht, A. Jakubek, P. Ebbinghaus and M. Rabe, *Nanoscale*, 2026, DOI: 10.1039/D5NR03300D.
12 L. Wang, U. S. Schubert and S. Hoeppener, *Chem. Soc. Rev.*, 2021, **50**, 6507–6540.
13 A. Dazzi, F. Glotin and R. Carminati, *J. Appl. Phys.*, 2010, **107**, 124519.
14 D. Nowak, W. Morrison, H. K. Wickramasinghe, J. Jahng, E. Potma, L. Wan, R. Ruiz, T. R. Albrecht, K. Schmidt, J. Frommer, D. P. Sanders and S. Park, *Sci. Adv.*, 2016, **2**, e1501571.
15 Q. Xie and X. G. Xu, *Langmuir*, 2023, **39**, 17593–17599.
16 R. W. Vook, *Opt. Eng.*, 1984, **23**, 343–348.
17 Y. Zhang, U. Yilmaz, G. V. B. Lukasievicz, L. O'Faolain, B. Lendl and G. Ramer, *Proc. Natl. Acad. Sci. U. S. A.*, 2025, **122**, e2403079122.
18 H. Hoffmann, U. Mayer and A. Krischanitz, *Langmuir*, 1995, **11**, 1304–1312.

19 J. A. Mielczarski, *J. Phys. Chem.*, 1993, **97**, 2649–2663.

20 Y. Jeon, J. Sung, C. Seo, H. Lim, H. Cheong, M. Kang, B. Moon, Y. Ouchi and D. Kim, *J. Phys. Chem. B*, 2008, **112**, 4735–4740.

21 A. Dhotel, Z. Chen, J. Sun, B. Youssef, J.-M. Saiter, A. Schönhals, L. Tan and L. Delbreilh, *Soft Matter*, 2015, **11**, 719–731.

22 R. L. Olmon, B. Slovick, T. W. Johnson, D. Shelton, S.-H. Oh, G. D. Boreman and M. B. Raschke, *Phys. Rev. B:Condens. Matter Mater. Phys.*, 2012, **86**, 235147.

23 D. W. Lynch and W. Hunter, *Introduction to the Data for Several Metals*, Elsevier, 1997, pp. 233–286.

24 D. Chandler-Horowitz and P. M. Amirtharaj, *J. Appl. Phys.*, 2005, **97**, 123526.

25 J. Kischkat, S. Peters, B. Gruska, M. Semtsiv, M. Chashnikova, M. Klinkmüller, O. Fedosenko, S. Machulik, A. Aleksandrova, G. Monastyrskyi, Y. Flores and W. T. Masselink, *Appl. Opt.*, 2012, **51**, 6789.